



1 **Relation between total-column and near-surface NO₂ based on in-**
2 **situ and PANDORA ground-based remote sensing observations**

3
4 **Ying Zhang^{a,b}, Yuanyuan Wei^{c*}, Gerrit de Leeuw^{a,d}, Ouyang Liu^{a,b}, Yu Chen^e,**
5 **Yang Lv^a, Yuanxun Zhang^b, Zhengqiang Li^{a,b}**

6
7 *^a State Environmental Protection Key Laboratory of Satellite Remote Sensing,*
8 *Aerospace Information Research Institute, Chinese Academy of Sciences, Beijing,*
9 *100101, China*

10 *^b University of Chinese Academy of Sciences, Beijing 100049, China*

11 *^c Changcheng Institute of Metrology & Measurement, Beijing, 100095, China*

12 *^d R&D Satellite Observations, Royal Netherlands Meteorological Institute (KNMI),*
13 *3730AE De Bilt, the Netherlands*

14 *^e CMA Public Meteorological Service Centre, Beijing 100081, China*

15
16 *Yuanyuan Wei

17 Corresponding author at the Changcheng Institute of Metrology & Measurement.

18 Address: Huanshan Village 108, Haidian District, Beijing, China

19 Postcode: 100095

20 Email: weiy020@avic.com

21



22 **Abstract**

23 Nitrogen dioxide (NO₂) is a major pollutant which at high concentrations may affect
24 human health. It is also a photochemically reactive gas which is important for the
25 oxidation potential of the atmosphere and acts as a precursor for the formation of
26 aerosol particles and ozone. However, monitoring of near-surface (NS) NO₂ faces the
27 challenge of spatial discontinuity due to large distances between ground-based
28 monitoring stations, whereas satellite remote sensing provides column-integrated
29 concentrations (total column, TC) which are related to NS concentrations in a
30 complicated manner. In this study, the relation between TC and near-surface (NS) NO₂
31 concentrations is studied using TC NO₂ data from remote sensing observations using a
32 Pandora and NS NO₂ concentrations from in-situ observations, which were located at
33 the Beijing-RADI site (Beijing, China) during January 2022. The ratio between TC and
34 NS NO₂ concentrations varies throughout the day with substantially different relations
35 in the morning and afternoon. During the night and morning the atmosphere was
36 vertically stratified, with disconnected layers which prevented vertical mixing of
37 atmospheric constituents. In the afternoon, these layers connected allowing for vertical
38 mixing and transport between the surface and the top of the boundary layer. Thus the
39 prohibition of vertical transport in the morning and the mixing in the afternoon resulted
40 in different relations between the NS and TC NO₂ concentrations. These different
41 relationships have consequences for the use of satellite remote sensing to estimate NS
42 NO₂ concentrations.

43

44 **Keywords:** Nitrogen dioxide, remote sensing, air pollution, Beijing, winter

45



46 **1 Introduction**

47 Nitrogen dioxide (NO₂) can have adverse effects on human health (Eum et al.,
48 2022, 2019; Nordeide Kuiper et al., 2021; Kornartit et al., 2010). NO₂ plays an
49 important role in atmospheric chemistry, and acts as a precursor for the formation of
50 ozone and secondary aerosols in the atmosphere. The major sources of NO₂ are from
51 fossil fuel burning such as power plants, traffic and households. Because of these
52 anthropogenic sources, together with the relatively short atmospheric lifetime of NO₂,
53 high tropospheric NO₂ concentrations are usually observed near highly industrialized
54 regions (Van der A et al., 2006), densely populated agglomerations (de Souza et al.,
55 2022), and power plants (Tang et al., 2024), as well as along major highways (Goldberg
56 et al., 2021) and shipping lanes (Ding et al., 2018). In addition, NO₂ is produced from
57 some natural sources such as lightning and soil emissions.

58 Concentrations of NO₂ in the atmosphere can be measured using satellite-based
59 sensors providing vertical total column and tropospheric densities, ground-based
60 remote sensing using MAX-DOAS or Pandora instruments, or in situ instruments.
61 Satellite remote sensing is currently a widely used technique, for example using the
62 Ozone Monitoring Instrument (OMI, Levelt et al., 2006) on the Aura satellite, and the
63 TROPOspheric Monitoring Instrument (TROPOMI, Veefkind et al., 2012) on the
64 Sentinel-5 Precursor (S5P) satellite. Satellite data show that the total column (TC) NO₂
65 concentrations are highly variable in space and time (e.g., Lamsal et al., 2014; Fan et
66 al., 2021). Duncan et al. (2016) analyzed global NO₂ observed by OMI from 2005-2014
67 and found that NO₂ levels were initially high over China but had significantly decreased
68 over the Beijing, Shanghai and the Pearl River Delta (PRD) regions in 2014, in response
69 to pollution control measures. In particular, over the PRD region the NO₂
70 concentrations decreased by about 40%. Also in the following years, the NO₂
71 concentrations over China have been substantially reduced in response to the
72 implementation of emission reduction policy (e.g. van der A et al., 2017; Fan et al.,
73 2021; de Leeuw et al., 2021) and fell below the 2008 level in 2017 (Zhao et al., 2023).
74 However, the decrease seems to have flattened in recent years (Fan et al., 2021).



75 The Pandonia Global Network (PGN) of Pandora Spectrometer Instruments has
76 been established in 2018 (<http://www.pandonia-global-network.org/>, last accessed:
77 10th July 2024) to provide “quality observations of total column and vertically resolved
78 concentrations of a range of trace gases”. The PGN data are used, for instance, for the
79 validation of products from environmental satellites. However, the comparison of OMI
80 TC NO₂ data with Pandora observations at 6 sites in Korea and the USA by Herman et
81 al. (2019) showed that mean and daily Pandora NO₂ concentrations were 50% or more
82 higher than those retrieved from OMI at sites that were frequently contaminated, such
83 as Seoul, Busan and Washington DC. Tzortziou et al. (2018) reported that Pandora TC
84 NO₂ observations during the KORUS-AQ coastal cruise experiment (Tzortziou, et al.,
85 2015) were 10-50% higher than OMI-derived TC NO₂. Thompson et al. (2019), using
86 data from the same experiment, reported that there is no consistent correlation between
87 TC and NS NO₂ across different cases and that the relation between TC and NS NO₂ is
88 complex. Similar results were obtained from the analysis of data from the DISCOVER-
89 AQ campaign in the Baltimore-Washington region in July 2011; the discrepancies were
90 suggested to be caused by the large field of view of OMI (Flynn et al., 2014; Knepp et
91 al., 2015; Reed et al., 2015; Tzortziou et al., 2015). Preliminary validation of TC NO₂
92 observations from the Ozone Mapping and Profiler Suite (OMPS) aboard the joint
93 NASA/NOAA Suomi National Polar-orbiting Partnership (Suomi NPP) satellite by
94 Huang et al. (2022) in the USA showed that OMPS TC NO₂ tends to be lower in
95 polluted urban areas and higher in clean areas/events than Pandora observations.
96 Ialongo et al. (2020) and Zhao et al. (2020) obtained similar results from the validation
97 of TROPOMI TC NO₂ using PGN data but the differences were significantly smaller
98 than for the OMI and OMPS data with a coarser spatial resolution than TROPOMI. The
99 validation of TROPOMI TC versus Pandora data at the Beijing-RADI site shows the
100 good performance of TROPOMI (Liu et al., 2024). It is noted that Liu et al. re-sampled
101 the TROPOMI data to a spatial resolution of 100×100 m², i.e. similar to that of the
102 Pandora observation area.

103 Satellite-derived TC NO₂ data are often used to determine trends (e.g., van der A



et al., 2017; Fan et al., 2021) but, in view of the above, the relation between TC and NS NO₂ is more complex. For instance, Fan et al. (2021) discussed the TS/NS relationship for selected major urban regions in China during the first 20 weeks after the COVID-19 lockdown and observed substantial differences (their Figure 9). Chang et al. (2022) analyzed data from the Geostationary Environment Monitoring Spectrometer (GEMS) Map of Air Pollution (GMAP) campaign conducted during 2020–2021. Their results show that TC NO₂ and NS NO₂ are better correlated in advective boundary layer conditions at high wind speeds, with a more uniform vertical distribution of NO₂, than during mixed boundary layer conditions with plumes from large point sources decoupled from the surface or transported from nearby cities, enhancing the vertical heterogeneity of NO₂. Similarly, Liu et al. (2024) show different relations between TC and NS NO₂ for low and high concentrations which are qualitatively explained in terms of transport and local emissions. Thus, to accurately assess NO₂ pollution in China and effects on air quality, accurate ground-based observations are needed.

Although a large number of ground-based NO₂ observation stations have been established in China since 2012 by the China National Environmental Monitoring Center (CNEMC) of the Ministry of Ecology and Environment of China (MEE) for the provision of the ground-based monitoring data (available at <http://www.mee.gov.cn/>; last access: 08 July 2024), there are still large areas for which no data are available. Satellite data can fill these gaps by converting satellite observations of aerosols and trace gases from TC to NS concentrations. Such data are usually provided from sensors flying on polar-orbiting satellites with global coverage but with a single overpass per day which at most latitudes cannot provide the daily variability of NO₂ characteristics. However, with the launch of geostationary satellites, spatial and temporal distributions of NO₂ concentrations can be obtained within the satellite field of view throughout the day. The GEO-KOMPSAT-2B geostationary satellite, launched by the National Institute of Environmental Research (NIER) under the Ministry of Environment, Korea, in February 2020, carries the Geostationary Environment Monitoring Spectrometer (GEMS), which provides high-resolution measurements of TC concentrations of key



133 air quality components (Kim et al., 2020). With the launch of GEMS, the Asian region
134 was the first to achieve coordinated hour-by-hour monitoring of pollutants. GEMS will
135 form a constellation of satellites to monitor air quality globally with high temporal and
136 spatial resolution, together with the Tropospheric Emissions: Monitoring Pollution
137 (TEMPO) mission, launched by NASA on 7 April 2023 to cover the North American
138 region (<https://tempo.si.edu/overview.html>) and Sentinel-4 planned to be launched on
139 the Meteosat Third Generation Sounder (MTG-S) planned to be launched by the
140 European Organisation for the Exploitation of Meteorological Satellites (EUMETSAT)
141 in 2024 (EUMETSAT, 2024). Although geostationary satellites can make continuous
142 observations of TC NO₂ during the day, the difference between TC and NS NO₂ remains
143 an important challenge. The weak correlation between NS NO₂ concentrations and
144 satellite-derived TC NO₂ (Lamsal et al., 2014), is closely related to their vertical
145 distribution, lifetime in the atmosphere, and chemical reactions (Xing et al., 2017). To
146 study the relation between TC and NS NO₂, accurate information is needed on both the
147 TC NO₂ and the NO₂ vertical structure in the atmosphere, together with the temporal
148 evolution, which until recently was not available for China.

149 The first operational Pandora instrument in China has been installed at the Beijing-
150 RADI site in 2021, for the ground-based remote sensing of several trace gases (e.g.
151 NO₂). The Beijing-RADI Pandora instrument is part of the PGN network and all data
152 are publicly available via the PGN website ([https://data.pandonia-global-](https://data.pandonia-global-network.org/Beijing-RADI/Pandora171s1/)
153 [network.org/Beijing-RADI/Pandora171s1/](https://data.pandonia-global-network.org/Beijing-RADI/Pandora171s1/), last accessed: 22 Jan 2025) within one day
154 of the observations. The aim of this study is to analyze the relationship between TC
155 NO₂ obtained by remote sensing and NS measurements during a field experiment at the
156 Beijing-RADI site during January 10-29, 2022. In order to better determine and
157 understand the relation between TC and NS NO₂ concentrations, we also used auxiliary
158 data such as simultaneous measurements of PM_{2.5} mass concentrations, lidar
159 observations, meteorological parameters, and satellite observations. Section 2 presents
160 the experiments and data, Section 3 presents the main results, and the conclusions and
161 discussion are presented in Section 4.

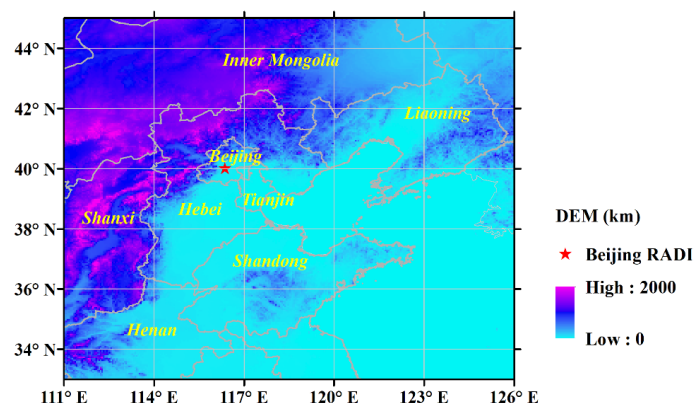


2 Materials and Method

2.1 Site description

Beijing is a metropolis with an area of 16,800 square kilometers and a population of nearly 22 million (2023) (<https://worldpopulationreview.com/world-cities/beijing-population>, last accessed: 22 Jan 2025). Beijing is surrounded by high mountains to the north, east, and west (Figure 1). The rapid economic development of Beijing and the topography of the area lead to emission of pollutants which may either disperse or accumulate, depending on wind direction and wind speed. During northwesterly winds, clean air is transported from the mountains, whereas during southerly winds polluted air is transported from the highly industrialized North China Plain. The southerly airflow is blocked by the mountains to the west and north and thus pollution accumulates, in particular during certain weather conditions conducive for the formation of smog, such as low wind speed. Photochemical processes may further contribute to the build-up of pollution which may result in the formation of haze.

The Beijing_RADI site is located at the roof (22 m above the surface) of the Aerospace Information Research institute of the Chinese Academy of Sciences (40.004° N, 116.379° E, elevation 59 m), which in turn is located in the north of Beijing between the Fourth and Fifth Ring Roads at the edge of the Olympic Parc. The site is representative for an urban background affected by vehicle exhaust, combustion and domestic emissions including those from heating during wintertime.





183 **Figure 1.** Digital elevation map of the study area showing the location of the Beijing-
 184 RADI site (40.004° N, 116.379° E, altitude at 59 m) (red star) and surrounding
 185 mountains.

186 A short-term field experiment was carried out at the Beijing-RADI long-term
 187 observation site during January 10-29, 2022. Pandora provided TC and NO_2
 188 concentrations in 4 layers, information on the spatial distribution of TC NO_2 was
 189 obtained from TROPOMI and a lidar provided aerosol backscatter profiles showing the
 190 vertical structure and evolution of the atmospheric boundary layer. The NS parameters
 191 were measured with instrumentation mounted near the Pandora on the roof of the
 192 AirCAS building, as described in the following sections.

193 **2.2 Observations of Column-Integrated Parameters and Vertical Profiles**

194 **2.2.1 Pandora**

195 Pandora is a UV-visible spectrometer which can provide high-quality
 196 measurements of spectrally resolved direct-sun/lunar or sky scan radiances. It uses
 197 direct solar measurements to obtain TC NO_2 , and sky measurements to obtain the
 198 vertical layer concentrations of NO_2 , with a FOV of 2.6° in direct sun mode and 1.5° in
 199 sky mode (Cede et al., 2024). Based on the Beer-Bouguer-Lambert law, the spectra
 200 observed at 400–470 nm in direct-sun mode are used to invert TC NO_2 using the
 201 differential optical absorption spectroscopy (DOAS) technique of trace gas spectral
 202 fitting. Pandora's direct sun measurements depend only on the geographic location with
 203 a known solar zenith angle which simplifies the air mass factor for correction of the
 204 atmospheric light path (Chang et al., 2022). Pandora measures TC NO_2 with a clear-sky
 205 precision of 0.01 DU and a nominal accuracy of 0.1 DU Herman et al. (2009). In view
 206 of this high precision, we use TC NO_2 in this study and select products with quality
 207 control flag of L10. Diffuse (scattered) radiation is measured at 5 pointing zenith angles
 208 (PZAs) in sky mode which, together with the direct sun measurement, provides
 209 information on the tropospheric VCD and on the surface concentrations. The PZAs are
 210 0° , 60° , 75° , 88° and a maximum angle taken as 89° . The measurements are taken in a



211 V shape (all angles are measured twice around a central angle) as described in Cede
 212 (2021). These data are used to derive vertical profiles as described in the ATBD (Cede,
 213 2024) Section 6.7, which were downloaded from the PGN website. Pandora data are
 214 public and can be downloaded from the PGN website ([https://pandonia-global-](https://pandonia-global-network.org)
 215 [network.org](https://pandonia-global-network.org), last accessed: 22 Jan 2025).

216 **2.2.2 Lidar**

217 A small lidar developed by the Hefei Institute of Physical Sciences, Chinese
 218 Academy of Sciences, was used for continuous measurements of aerosol backscatter
 219 profiles during day and night. The GBQ L-01 aerosol lidar consists of a laser, optical
 220 unit, control unit board, high-speed signal acquisition card, industrial motherboard and
 221 communication module. The GBQ L-01 aerosol lidar uses a high-frequency pulse laser
 222 emitting linearly polarized light at a wavelength of 1064nm. The optical unit consists
 223 of a transmitter and a receiver. The optical transmitter unit emits laser light pulses,
 224 which are expanded before they are emitted into the atmosphere. The optical receiver
 225 unit consists of a telescope which focuses the back-scattered light onto an optical
 226 detector which in turn is connected to an amplifier unit. The vertical and parallel
 227 polarized components of the back-scattered light are separated by the polarizing prism
 228 in the receiving channel. The industrial motherboard carries lidar acquisition and
 229 control software and data analysis software to control the overall operation of the
 230 system.

231 **2.2.3 TROPOMI**

232 The TROPOMI (TROPOspheric Monitoring Instrument) is a passive-sensing
 233 hyperspectral nadir-viewing imager aboard the Sentinel-5 Precursor (S5P) satellite,
 234 launched on 13 October 2017. S5P flies at an altitude of 817 km in a near-polar sun-
 235 synchronous orbit. The local equator overpass time in the ascending node is 13:30, and
 236 the repetition period is 17 days (KNMI, 2017). TROPOMI's four separate
 237 spectrometers cover wavelengths in the ultraviolet (UV), UV-visible (UV-VIS), near-
 238 infrared (NIR) and short wavelength infrared (SWIR) spectral bands (Veefkind et al.,
 239 2012). The TC NO₂ used in this study is derived from spectral measurements of solar



240 radiation in TROPOMI's UV–VIS wavelength bands (van Geffen et al., 2015, 2019).
241 Compared to the relatively small field-of-view of the Pandora instrument, the size of
242 the TROPOMI ground pixel (3.5 km × 5.5 km; across × along track) is relatively large.
243 Therefore, TROPOMI NO₂ products are only used as a reference for upwind
244 concentrations during backward trajectory tracking and not for quantitative analysis.
245 Furthermore, tropospheric NO₂ column densities are used because these are more
246 representative of near-surface NO₂.

247 **2.3 Near Surface Measurement**

248 **2.3.1 Trace Gas Analyzer**

249 The Thermo Fisher Scientific Model 42i Trace Level Chemiluminescence NO-
250 NO₂-NO_x Analyzer was used to measure NS NO₂ concentrations. This instrument first
251 transforms NO₂ into nitric oxide (NO) using a molybdenum NO₂ to NO converter
252 heated to about 325 °C. Then, NO and ozone (O₃) react to produce a characteristic
253 luminescence with an intensity linearly proportional to the NO concentration (Model
254 42i Trace Level Manual, 2007). NO₂ values are derived by subtracting NO from NO_x
255 measurements. Measurements were made every minute during the observation period.

256 **2.3.2 Beta attenuation monitor**

257 Ground-based near-surface PM_{2.5} concentrations were measured using the beta
258 attenuation monitor Met One BAM-1020 (BAM 1020 particulate monitor operation
259 manual) equipped with a PM_{2.5} inlet. The Met One BAM-1020 collects aerosol particles
260 on glass filter tape. PM_{2.5} is measured using beta rays generated by a small ¹⁴C source
261 (<https://metone.com/products/bam-1020/>). At the start of every measurement cycle, the
262 flux of beta rays is measured across clean filter tape, to determine a zero reading. Next,
263 the filter tape is advanced and ambient air is sampled at the same spot, with a controlled
264 air flow, thereby impregnating the tape with PM_{2.5}. After the sampling is completed, the
265 tape retracts and PM_{2.5} samples are dried (in an environment with relative humidity
266 lower than 40% which removes most of the water content) by a built-in heater. Then
267 the concentration of PM_{2.5} collected on the filter tape is measured as described above.
268 Samples are taken every hour.



269 **2.3.3 Auxiliary meteorological data**

270 In addition to the above observations, we also use weather maps, meteorological
271 surface observations and sounding observations published by the World Meteorological
272 Organization (WMO) to aid in our analyses. Weather maps for the Asian region are
273 published by the Korea Meteorological Administration and can be downloaded at
274 http://222.195.136.24/chart/kma/data_keep (last accessed: 22 Jan 2025). We
275 downloaded the surface and sounding observations of meteorological station 54511 in
276 Beijing, located at 39.93N, 116.28E, which is part of the WMO network. These data
277 are available from the website of the University of Wyoming
278 (<http://weather.uwyo.edu/surface/>) (last accessed: 22 Jan 2025). Although this station is
279 far away from our experimental site (about 23 km), it is representative of the
280 macroscopic changes of the meteorological conditions in Beijing.

281 **2.4 HYSPLIT Model**

282 To better understand the regional transport pathways and source regions at
283 different altitudes, backward trajectories from the Hybrid Single Particle Lagrangian
284 Integrated Trajectory (HYSPLIT; Draxler & Hess, 1998) model were used. The
285 HYSPLIT model assumes that the parcel trajectory is formed through time integration
286 and spatial differences when moving in the wind field. The path of the air mass is mainly
287 related to the air flow situation, pressure system movement and topography (Draxler &
288 Hess, 1998). The HYSPLIT model has the ability to deal with a variety of
289 meteorological input fields and physical processes, and can also be used to describe
290 atmospheric transport, diffusion and deposition of pollutants and harmful substances
291 (Stein et al., 2015). In this study, the backward trajectories were initialized for arrival
292 at the Beijing-RADI site at 300, 500 m, and 1000 m. The HYSPLIT model was run at
293 https://www.ready.noaa.gov/HYSPLIT_traj.php, with the input meteorological field
294 data (0.25°×0.25°) provided by the Global Forecasting System.



295 **3 Results and Analysis**

296 **3.1 Data overview**

297 Time series of the measured NS and TC concentrations of NO₂ during the study
 298 period are presented in Fig. 2a. For comparison of NS NO₂ concentrations with Pandora
 299 observations, they are expressed in mg m⁻³. Fig 2a shows the common diurnal variation
 300 of the NO₂ concentrations, i.e. a gradual decrease in the morning to a minimum around
 301 mid-day, followed by a gradual increase in the afternoon to a maximum value during
 302 the night. This diurnal variation is due to photochemical reactions during daytime,
 303 meteorological effects and anthropogenic emissions during certain hours (for instance
 304 during rush hour) (e.g., Atkinson, 2000; Boersma et al., 2009; Y. Zhang et al., 2016;
 305 Cheng et al., 2018; Li et al., 2021). TC NO₂ concentrations can only be measured with
 306 Pandora during day time. The diurnal variations between 8:00 and 16:00 local Beijing
 307 time (UTC+8; throughout this paper local time, LT, will be used) at the Beijing-RADI
 308 side are similar to those of NS NO₂. Based on the variation of the NS NO₂
 309 concentrations (Fig. 2a) three periods are considered during the study period: Period I:
 310 10 to 18 January, with strong diurnal variations and high NO₂ concentration peaks;
 311 Period II: 19 to 24 January, NS NO₂ sharply decreases and then increases with stronger
 312 fluctuations, but TC NO₂ observations are not available due to the presence of clouds;
 313 Period III: 25 to 30 January, a sudden drop occurred on January 25, and low NO₂
 314 concentrations with some narrow peaks lasted until the 30th.

315 The time series of the NS PM_{2.5} concentrations in Fig. 2b shows four peaks in
 316 Period I, with maximum values during the night and very low concentrations (<10 µg
 317 m⁻³) during daytime. The maxima were relatively low on 12 and 17 January (~25 µg
 318 m⁻³), whereas on 14 and 18 January the PM_{2.5} peak concentrations were ~120 and ~70
 319 µg m⁻³. During Period II, the PM_{2.5} concentration increased steadily from less than 25
 320 µg m⁻³ on 20 January to more than 125 µg m⁻³ on the 24th, with similar day/night
 321 variations as in Period I. During Period III, the PM_{2.5} concentrations were relatively
 322 low (<25 µg m⁻³) and there was no clear diurnal variation.



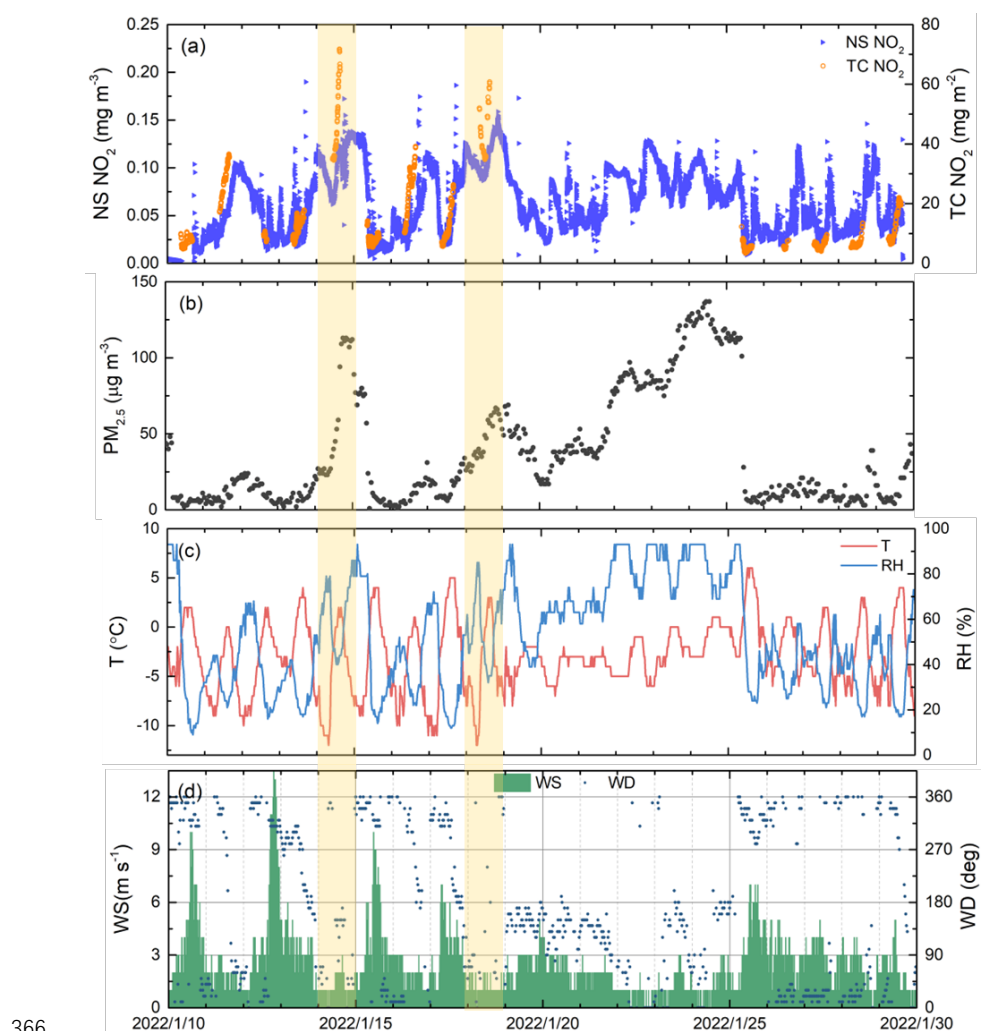
323 The air temperature and relative humidity (RH) during the study period are
 324 presented in Fig. 2c and the wind speed and wind direction are presented in Fig. 2d.
 325 During Period I, air temperature, RH and wind speed all varied strongly with a clear
 326 diurnal pattern: elevated wind speed during the day, with daily maxima between about
 327 7 and 13 m s⁻¹, and very low wind speed during the night (<2 m s⁻¹); day time air
 328 temperatures around 0°C and night time temperatures around -10°C; dry air during the
 329 day (RH~20%) and more humid during the night (RH of 60-80%). The wind was mostly
 330 from northerly directions (NW-NE) and veering during the night. During Period II, the
 331 air temperature increased gradually from about -5°C to about 0°C, with small diurnal
 332 variations, and RH increased initially from 40% to 60% on 20 January and then
 333 gradually to about 70%, with little day/night variations, whereas during the nights of
 334 22-25 January the humidity was very high, the RH sensor saturated and reported
 335 maxima close to 100%. Wind speed during this period was low (< 3 m s⁻¹) and wind
 336 direction was mostly SE. During period III, day/night temperature and RH fluctuations
 337 occurred, with day time air temperatures above 0°C and gradually rising and RH
 338 varying between 20% during the day and 60% during the night. Wind speeds were
 339 higher during the day, mostly a little higher than 3 m s⁻¹, than during the night (close to
 340 0 m s⁻¹) and wind direction was mostly northerly.

341 The variations of the NO₂ and PM_{2.5} concentrations were similar in the sense that
 342 the minimum and maximum peak concentrations occurred at about the same time, but
 343 with differences in the ratios between minima and maxima. The occurrence of peak
 344 concentrations during the night is consistent with the variation in meteorological
 345 conditions, with maxima during low wind speed and low air temperature, conducive for
 346 the formation of a nocturnal boundary layer in which the concentrations accumulate
 347 near the surface. This is observed during Periods I and III. During Period II, however,
 348 there were no Pandora observations during day time due the occurrence of clouds. This
 349 suggests that clouds may also have been present during the night. Hence radiative
 350 cooling was reduced and air temperature did not decrease as much as during the other
 351 periods. Wind speed was low, thus pollutants were not transported away and



352 accumulated in the area, as also indicated by the high RH. Hence the concentrations of
353 NO₂ and PM_{2.5}, as well as RH, gradually increased during period II, with relatively
354 small diurnal variations.

355 For further analysis, we selected two cases for which both TC and NS NO₂ data
356 were available, including lidar observations and air mass trajectories. The selected cases
357 are the periods when both NO₂ and PM_{2.5} concentrations were high, i.e. on 14 and 18
358 January, when the 24-hour average NO₂ concentrations exceeded 80 mg m⁻³. The first
359 pollution episode (case 1) started in the afternoon of January 14 and ended in the
360 morning of January 15. The other pollution episode with high NS NO₂ occurred on
361 January 18 (case 2). The diurnal variation of the NS NO₂ concentrations was similar in
362 both cases, while the air temperature, RH, wind speed and wind direction show that
363 also the meteorological situations were similar. However, differences are observed in
364 the temporal variations of TC NO₂ concentrations versus NS NO₂ concentrations and
365 in PM_{2.5} concentrations.



366

367 **Figure 2.** Time series of observed parameters from Jan 10 to 29, 2022 (a) TC and NS
 368 NO₂ concentrations, (b) NS PM_{2.5} concentration, (c) temperature and related humidity,
 369 and (d) wind speed and wind direction from WMO meteorological station 54511 in
 370 Beijing.

371 3.2 Variations of TC and NS NO₂ during the two selected cases

372 The evolution of the TC and NS NO₂ concentrations and their ratio during the two
 373 high pollution episodes identified in Section 3.1 are discussed in detail. Processes
 374 influencing the concentrations and their ratio are identified based on lidar data,



375 providing information on the boundary layer structure, together with large scale
 376 weather maps and air mass trajectory analyses, providing information on sources of
 377 pollutants and their transport over a wider area.

378 **3.2.1 Case 1: Disconnected boundary layers merging (14 January, 2022)**

379 Time series of the TC and NS NO₂ concentrations on 14 January 2022 (Fig. 3a)
 380 show their different evolution throughout the day. The NS NO₂ concentrations are
 381 available for every minute during the whole day and show a gradual decrease from
 382 about 0.11 mg m⁻³ between midnight and 04:00 to about 0.065 mg m⁻³ at 10:30. After
 383 10:30 the concentrations increased to 0.11 mg m⁻³ at 13:30 and hardly changed until
 384 about 16:00 after which they strongly fluctuated (0.04-0.175 mg m⁻³) and then reached
 385 a steady value of about 0.12 mg m⁻³ from 19:00 till midnight. The strong fluctuations
 386 may have been caused by emissions during evening rush hour, domestic heating and
 387 other activities producing NO₂, followed by stabilization during the evening.

388 Pandora uses direct sun observations and during this campaign in the winter time,
 389 high quality TC NO₂ data are only available between 10:30 and 15:30. The data in Fig.
 390 3a show initially a similar behavior of TC and NS NO₂ concentrations, with little
 391 variation between 10:30 and 11:30. Thereafter, both NS and TC concentrations
 392 increased, initially slower for the TC than for the NS concentrations. After 13:00 the
 393 NS concentrations levelled off while the TC concentrations increased much faster.
 394 Between 12:00 and 15:00 the TC concentrations increased from 40 mg m⁻² to 72 mg m⁻²,
 395 almost a doubling, then decreased to 64 mg m⁻². The difference in the temporal
 396 behavior between the TC and NS NO₂ concentrations is amplified in Fig 3b which
 397 shows a scatterplot between the TC and NS concentrations. Observations before and
 398 after 13:00 are plotted with different symbols and color coded in blue and red,
 399 respectively. For each of these two data sets, before and after 13:00, TS and NS
 400 concentrations are well correlated with linear correlation coefficients R of 0.94 and 0.85,
 401 respectively, but with significantly different slopes.

402 The different behavior of the TC and NS NO₂ concentrations can be explained by



403 considering the dynamical behavior of the boundary layer structure. Lidar observations
404 reveal the vertical structure of the atmospheric boundary layer from the variation of the
405 lidar signal as a function of height. A 3-D plot of the vertical variation of the lidar signal,
406 measured on 14 January 2022 at the Beijing-RADI site, close to the Pandora and the
407 ground-based measurements, is presented in Fig. 3c. The lidar signals are color-coded
408 according to the scale to the right of Fig. 3c and each vertical line shows the variation
409 of the lidar signal with height, plotted along the primary vertical axis. The time of
410 measurement of each profile is plotted along the horizontal axis. The lidar signal in this
411 figure is range-corrected, i.e. corrected for attenuation as the laser light propagates in
412 the atmosphere away from the emitter and, after backscattering by aerosol particles,
413 back to the receiver. The time between emission of the laser pulse and receiving the
414 backscattered signal is a measure for the height where the backscattering takes place
415 (after correction of the slant to a vertical optical path) and the intensity is a measure for
416 the aerosol concentration. This is illustrated with the data in Fig 3d. For example, the
417 data show an aerosol layer between 08:00 and 13:00, located at a height between about
418 800 and 900 m, as indicated by the large lidar signal (yellow and red, i.e., between about
419 1.2 and 2.2), with light blue above and below, indicating lower aerosol concentrations.
420 Between about 400 and 500 m a dark blue area can be observed, which indicates very
421 low backscatter and thus the absence of aerosol, whereas further down toward the
422 surface, backscatter is observed with a varying intensity. The vertical variation of the
423 lidar signal, i.e. indicating the presence of aerosol in the layer adjacent to the surface
424 up to about 400 m, a layer with no aerosol between 400 and 500m and an elevated
425 intense aerosol layer above, indicates a situation of a disconnected boundary structure
426 with two layers which are not connected and thus no material can be exchanged
427 between these layers. Such a situation can occur due to nocturnal cooling when the
428 surface is cold due to radiation cooling and cools the layer adjacent to the surface (Stull,
429 1988). In this layer, no mixing occurs and material emitted near the surface accumulates.
430 The atmospheric trace gases and aerosol in the warmer layer above are trapped in that
431 layer and exchange with the cold layer below is prohibited due to the temperature



432 gradient. Hence the two layers become disconnect and may separate.

433 The occurrence of such a situation is consistent with the observations discussed in
434 Section 3.1 and Fig. 2, with low wind speed, lowest air temperature during period I (-
435 12°C) and enhanced RH (indicating trapping of water vapor together with decreased air
436 temperature). Also the lidar data in Fig. 3c indicate the occurrence of such a situation,
437 with a well-mixed shallow boundary layer between midnight and 03:00, an indication
438 of an internal boundary layer starting to form after about 04:00, disconnected from the
439 layer above. The internal boundary layer rises gradually until about 11:00, with the
440 clean layer above, and a new layer appears around 07:00, probably due to advection.
441 Note that wind direction was south-easterly during a short period of time on 14 January
442 with a wind speed of 2 m/s, slightly more than during the rest of the day when the wind
443 direction was northerly. During south-easterly winds, polluted air may be advected to
444 the Beijing-RADI site, whereas during northerly wind clean air is advected (Liu et al,
445 2024).

446 From 12:00, the lower layer deepened and backscatter is observed from the clean
447 layer indicating that aerosol is gradually mixed into that layer which completely
448 disappears around 14:00. At the same time, the lidar signal from the growing lower
449 layer increases gradually whereas after 13:00 the lidar signal from the upper layer
450 becomes smaller, indicating that the aerosol concentration becomes lower until both
451 layers are mixed around 14:00 into a well-mixed boundary layer. After 15:00, the lidar
452 signal increases, first near the surface and then growing throughout the boundary layer.
453 The increase of the NS concentrations is consistent with the highest PM_{2.5}
454 concentrations as presented in Fig. 2b and the overall increase of the lidar signal,
455 indicating increasing aerosol concentrations. This is confirmed by AERONET AOD
456 observations at the Beijing-RADI site ([https://aeronet.gsfc.nasa.gov/cgi-](https://aeronet.gsfc.nasa.gov/cgi-bin/data_display_aod_v3?site=Beijing_RADI&nachal=2&level=2&place_code=10)
457 [bin/data_display_aod_v3?site=Beijing_RADI&nachal=2&level=2&place_code=10](https://aeronet.gsfc.nasa.gov/cgi-bin/data_display_aod_v3?site=Beijing_RADI&nachal=2&level=2&place_code=10))
458 which however were only available until 16:00 LT.

459 The vertical variation of the NO₂ concentrations, derived from the Pandora sky

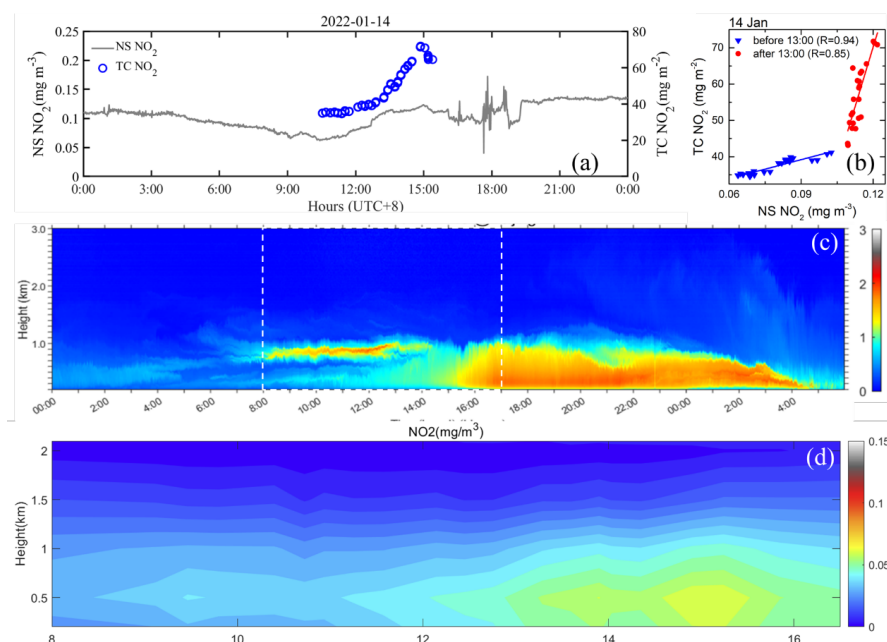


radiance measurements at four elevations, is presented in Fig. 3d. Pandora data are only available during day time and therefore only the period from 08:00-16:30 can be shown. The NO₂ concentrations are available in 4 layers. Assuming that NO₂ is uniformly distributed within each layer, the data were interpolated to form a time series of NO₂ vertical distributions, similar to the lidar profiles. The data in Fig. 3d also show the similar behavior of the NO₂ concentrations and the aerosol backscatter, with increasing concentrations between 12:00 and 17:00 and their vertical mixing. In particular the increase around 15:00 is evident in both the Pandora and lidar observations. However, the Pandora observations do not show the occurrence of disconnected boundary layers in the morning. Instead, the Pandora observations show an enhanced layer between 300-800 m, rather than the more detailed structure visible in the lidar data. These differences may be due to the absence of elevated NO₂ concentrations in the aerosol layer between 800 and 900 m, while the layered structure below is not well-resolved by Pandora due to its vertical resolution resulting in lower concentration over a large layer. The latter is in agreement with the observations later in the day.

The overall similarity between the variations in the lidar and Pandora observations supports the use of lidar observations to explain the dynamic behavior of the NO₂ concentrations. In particular, the different relations between TC and NS observations before and after 13:00 (Fig. 3b), can be explained by the occurrence of the disconnected layers. The variations of the NS NO₂ concentrations until 13:00 reflect the effects of chemical processes and emissions within the atmospheric layer near the surface and within the elevated layer where only removal processes influence the NO₂ concentrations. As a result, the temporal variation of the concentrations in both layers was in part influenced by the same processes, differences were not large (Fig. 3a) and the ratio of the TC/NS concentrations changed little (Fig. 3b). In the afternoon, such processes resulted in the increase of NO₂ concentrations while also the two layers are connected which, together with the somewhat enhanced wind speed (Fig 2d) resulted in mixing of NO₂ throughout the whole boundary layer up to about 1000 m. Hence the usual afternoon increase of NO₂ concentrations near the surface (Liu et al., 2024) was



489 dampened by upward transport whereas the increase in TC concentrations was
 490 enhanced, as is well illustrated by the time series of both NC and TC between 13:00
 491 and 15:00 (see Fig. 3a). As a result, also the TC/NS relationship changed substantially
 492 after 13:00 (Fig. 3b).

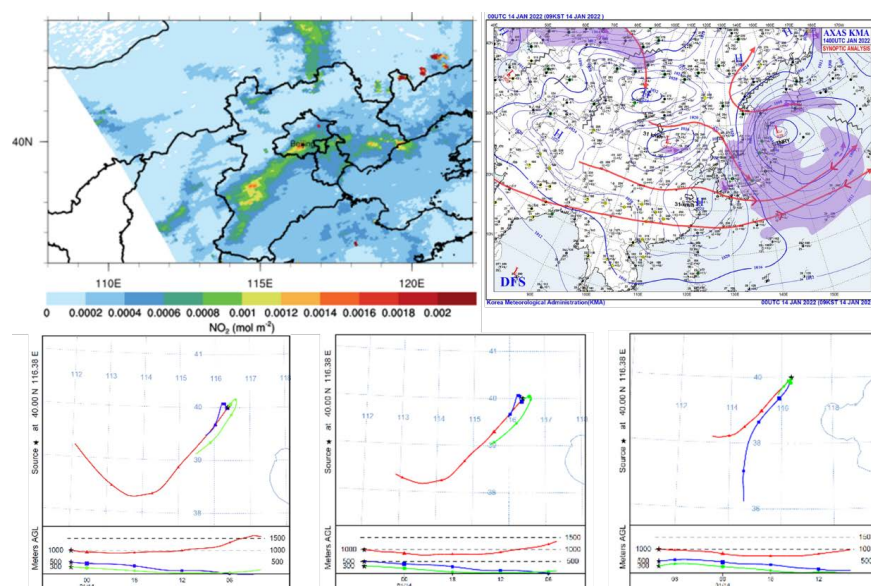


493
 494 **Figure 3.** (a) Time series of NS NO₂ (grey line) and TC NO₂ (blue circles) at the Beijing
 495 RADI site (40.004°N, 116.379°E) on Jan 14, 2022; (b) relationship between TC and
 496 NS NO₂ concentrations during the morning (before 13:00) and during the afternoon
 497 (after 13:00); (c) time series of vertical profiles of range-corrected lidar signal at 1064
 498 nm. Note that the lowest height in Fig. 3c is 100 m; (d) time series of NO₂ vertical
 499 profiles derived from Pandora sky radiance measurements.

500 The effect of transport on the NO₂ concentrations at the Beijing-RADI site on 14
 501 January 2022 was analyzed using the data presented in Fig. 4: the spatial distribution
 502 of tropospheric NO₂ columns derived from TROPOMI data (overpass time 13:30), the
 503 synoptic weather map at 00 UTC and 24-hour backward trajectories for arrival at the
 504 Beijing-RADI site at altitudes of 300 m, 500 m and 1000 m, at 10:00, 13:00 and 16:00
 505 LT. The TROPOMI data show the relatively high tropospheric NO₂ concentrations over



506 the study area, in particular over an elongated area stretching from the SW to the NE
507 over Hebei Province, including Beijing (compare with Fig. 1), and from Beijing
508 eastward. This area is bounded by the Taihang mountains in the west and by the Yan
509 mountains in the north, blocking transport of pollutants. The weather map in Fig. 4b
510 shows the pressure distribution and location of low pressure areas resulting in wind
511 from the SW, i.e. along the direction of the elongated area with elevated NO₂
512 concentrations (see Fig. 4a). This is confirmed by the air mass trajectories in Fig. 4c,
513 all showing overall transport from the SW. However, the trajectories arriving at 10:00
514 LT show that during the last 8h, the air mass arriving at 300 m came from the NE at
515 low wind speed and the airmass arriving at 500m came from the NW at even lower
516 windspeed. The airmass arriving at 1000 m came from the SW during the last 14 h
517 before arrival and from the NW during the earlier 12 hours. The airmasses arriving at
518 13:00 show similar trajectories. These trajectories are consistent with the lidar
519 observation of disconnected layers, with different air mass trajectories during the last
520 hours before arriving at the Beijing-RADI site and thus possibly different composition.
521 The air mass arriving at 1000 m had been at high elevations during its entire 24 h
522 trajectory and originated from higher than 1500m, but those arriving at 300 and 500 m
523 originated from the surface at different locations separated by tens of km and may thus
524 have been influenced by different sources.



525

526 **Figure 4.** (a) Spatial distribution of tropospheric NO₂ in the study area derived from
 527 TROPOMI data on 14 January 2022; (b) Synoptic weather map at 00:00 UTC (08:00
 528 LT); (c) 24-hour backward air mass trajectories arriving at the Beijing-RADI site at
 529 10:00, 13:00 and 16:00 LT, at heights of 300, 100 and 1000 m, calculated using the
 530 HYSPLIT model with 6h time steps (00, 06, 12 and 18) and a shorter time step to the
 531 arrival time.

532 3.2.2 Case 2: Multi-layer structure on 18 January, 2022

533 Time series of the TC and NS NO₂ concentrations on 18 January 2022 are shown
 534 in Fig. 5a, together with a scatterplot between the TC and NS concentrations in Fig. 5b
 535 and 3-D plots of the vertical variation of lidar backscatter coefficients in Fig. 5c and of
 536 NO₂ concentrations in Fig. 5d. The NS NO₂ time series in Fig. 5a show that the
 537 concentrations were higher than on 14 January, but their variation was initially similar,
 538 with a decrease to a minimum around 11:30 (later than on the 14th) followed by an
 539 increase. However, on 18 January, the increase continued non-linearly until about 14:30
 540 when the concentrations plateaued at a value of about 0.12 mg m⁻³ during about 1 hour
 541 and then increased further, likely due to increased emissions during rush hour and



decreasing photochemical sink when the solar radiation intensity decreased in the afternoon. After 18:00 the concentrations plateaued at $0.13\text{--}0.14\text{ mg m}^{-3}$, fluctuated up to about 0.14 mg m^{-3} around 21:00 and decreased somewhat toward the end of the day.

The TC NO_2 concentrations decreased faster than on 14 January, from the initial 54 mg m^{-2} around 08:30 to the minimum of 36 mg m^{-2} around 12:30, with a smaller decrease after 11:00. Hence, similar to the situation on 14 January, the TC NO_2 concentrations initially decreased while also the NS NO_2 concentrations decreased, but in contrast to the 14th, after 11:30 the TC NO_2 concentrations continued to decrease while the NS NO_2 concentrations increased. As a result, there was no clear correlation between TC and NS NO_2 concentrations before 13:00, as on 14 January. These morning data could be separated into two groups, before 11:30, when there was no TC/NS relation, and after 11:30 where the data in Fig. 5b suggest a non-linear relation. Hence, in this situation, it may be difficult to determine NS NO_2 concentrations from satellite data. After 13:00, the TC NO_2 concentrations increased from about 37 mg m^{-2} to almost 60 mg m^{-2} at 16:30, with a plateau around 15:00. The scatterplot in Fig. 5b shows a good correlation between TS and NS NO_2 concentrations.

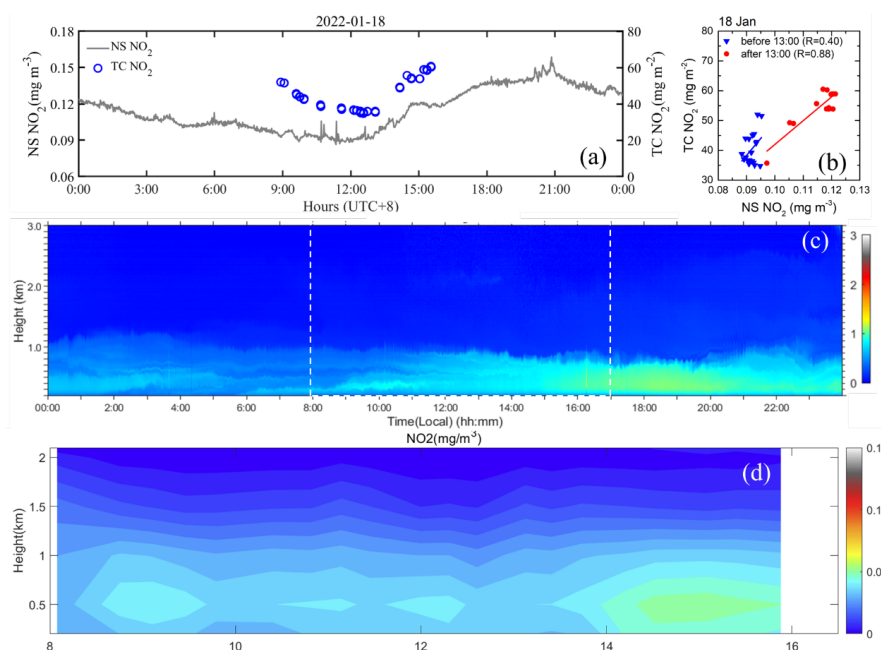
The lidar data in Fig. 5c, with lower intensity than on 14 January, indicate smaller aerosol concentrations on 18 January than on 14 January, consistent with the smaller $\text{PM}_{2.5}$ concentrations (in Fig. 2b). The lidar data show the occurrence of multiple layers during the night and morning, with sharp boundaries indicating that aerosol particles are trapped in rather shallow layers with little or no exchange between these layers. After 10:30, the boundaries between layers become less sharp indicating the onset of vertical transport, although the very shallow clear layer (dark blue) between 500 and 600 m indicates a clear separation between the lower and upper layers, prohibiting vertical transport. Around 13:00 this shallow layer disappeared and after 15:00 the atmospheric boundary layer appears well-mixed up to the top at about 800m.

The time series of the NO_2 vertical distributions in Fig. 5c shows that NO_2 concentrations were lower on the 18th than on the 14th, and concentrated below 1000 m.



570 The NO_2 concentrations and their vertical distributions varied between 08:00 and 12:30,
 571 with an initial increase between 08:00 and 10:00 with a broad elevated maximum
 572 centered around 500 m and another small maximum around 11, Apart from these, the
 573 NO_2 concentrations were rather homogeneously distributed up to the top of the
 574 atmospheric boundary layer at about 800 m as also indicated by the lidar data. After
 575 about 12:00 the NO_2 concentrations increased with a significant enhancement after
 576 14:00.

577 The evolution of the atmospheric boundary layer, as shown in detail by the lidar
 578 data, and the variation of the NO_2 concentration profiles provide a plausible explanation
 579 for the evolution of the TC and NS NO_2 concentrations and their ratios, with changes
 580 around 11:30 and 13:00. The plateau in the NS NO_2 concentrations may be indicative
 581 of the dilution near the surface due to upward transport and vertical mixing, at the same
 582 time increasing the TS NO_2 concentrations.



583
 584 **Figure 5.** Same as Fig. 3 but for 18 January, 2022.

585 Fig. 6 shows the large scale situation for the study area on 18 January. The TROPOMI
 586 data in Fig. 6a show the spatial distribution of the tropospheric NO_2 VCDs which are



587 highest to the SE of Beijing, in Hebei/Tianjin and over the Yellow Sea. Over Beijing,
588 the tropospheric NO₂ VCDs, as indicated by TROPOMI, are substantially lower than
589 in case 1. This can be explained by the transport from clean areas to the W and WNW
590 as indicated by the air mass trajectories arriving in Beijing at 300m, 500 m and 1000m,
591 at 10:00, 13:00 and 16:00 LT (Fig. 6c). The trajectories of the air masses arriving at
592 10:00 LT show a clear difference between the lower and higher layers visible in the
593 lidar data: where the air arriving at 1000 m originated from the WNW and had traveled
594 during the last 24 h over clean areas (Fig. 6a) over a distance of 1000 km (10°), between
595 heights of 1000-1500 m, the lower air mass was influenced by local air from SSW (at
596 300 m) and SW (500m) that had traveled during the last 24 h near the surface at heights
597 up to 500 m over moderately polluted areas. Hence the lidar data show higher aerosol
598 content in the lower layer (<500 m) than in the layer above (>600m) and both
599 disconnected layers are from different origin.

600 This situation changed as indicated by the air mass trajectory arriving at 12:00 LT. The
601 air mass arriving at 300 m had the same characteristics as at 10:00 LT, had traveled an
602 even shorter distance and the layer adjacent to the surface was more stagnant. However,
603 the air mass arriving at 500 m now came from the west, had traveled over clean areas
604 (Fig 6a) at heights between 500 and 1000 m and thus was distinctly different from the
605 layer below. The air mass arriving at 1000 m originated from a bit further north and
606 further away (in Inner Mongolia) than at 10:00 LT, and had travelled at heights between
607 750 and 1000 m. Hence all three air masses suggest that the layers originated from
608 different regions and likely had different composition.

609 The trajectories of the air masses arriving at 16:00 LT indicate that the situation had
610 changed, i.e. the pollution episode was finished and pollution was replaced with cleaner
611 air transported from the W to WNW over distances of hundreds of km and originating
612 from elevations of 500-1000 m for air masses arriving at 300m and 500m, whereas the
613 air mass arriving at 1000 m had actually followed a lower trajectory.

614

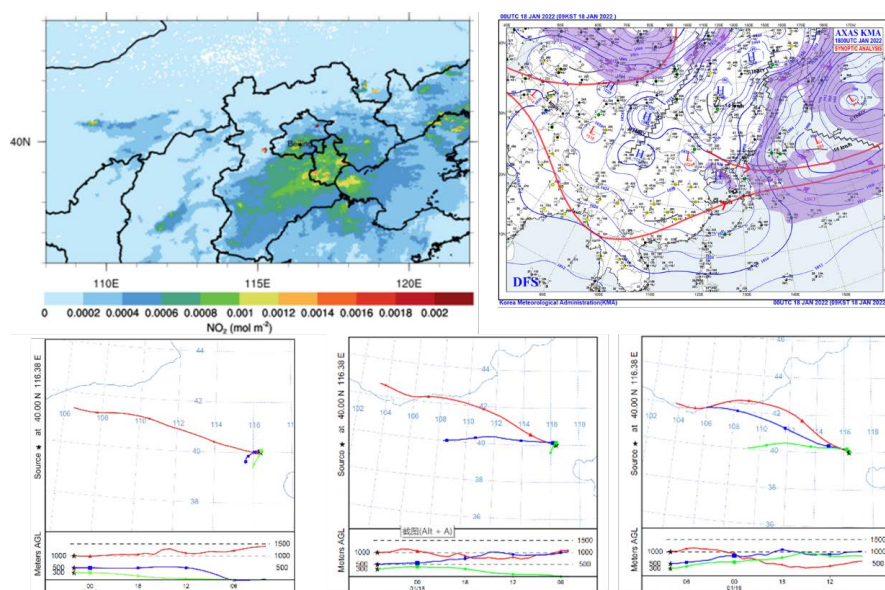


Figure 6. Same as Fig. 4, but for 18 January, 2022.

3.3 Ratio of TC vs NS NO₂

The two pollution cases discussed above show that the ratio between TC and NS NO₂ in the morning (before 13:00) is different from that in the afternoon (after 13:00) during the study period in the winter in Beijing. In order to better understand the relationship between TC and NS NO₂, we calculated the ratio of TC and NS NO₂ concentrations for each day, while we also differentiated between the morning and afternoon using 13:00 as the split time. The results are presented as violin plots in Fig. 7, for each of the 12 days for which data are available. The data in fig. 7 show that the mean and median values of the NO₂ ratio during Period I (10-18 January) were substantially higher than those during Period III (25-30 January), with the exception of 25 and 29 January. During these two days, at the beginning and end of Period III, signify the transition from polluted to clean days (see fig. 2b). On most days the ratio was smaller in the morning than in the afternoon. The difference between the morning and afternoon ratios was small during the two days (14th and 18th) with accumulated pollution, while during the four days when wind speed increased, on 13, 15, and 17, the differences were relatively large, with the largest difference of 192 m on the 13th.



During Period III the difference between the morning and afternoon ratio was basically smaller than 50 m, with a gap of more than 100 m only on the 29th. There were no valid observations of TC NO₂ concentrations during Period II, so it is not possible to judge the changes in ratio over multiple consecutive days of pollution. Throughout the observation period, the standard deviations of the ratio were overall larger in the morning than in the afternoon, when the winter boundary layer was well-mixed and the relationship between TC and NS NO₂ concentrations was relatively stable. However, in the morning, when the boundary layer was developing, the day-to-day variations in the standard deviation imply relatively large changes in the ratio. The box plot in fig. 7b illustrates the difference between the morning and afternoon ratios. The mean values are lower in the morning (364m) than in the afternoon (428m), and the upper quartile in the afternoon are closer to their median value, suggesting that the ratio is more stable in the afternoon when it is well mixed vertically. However, although the ratio is quite stable in the afternoon with well mixing, there are still unpredictable extreme values (e.g. 771 m).

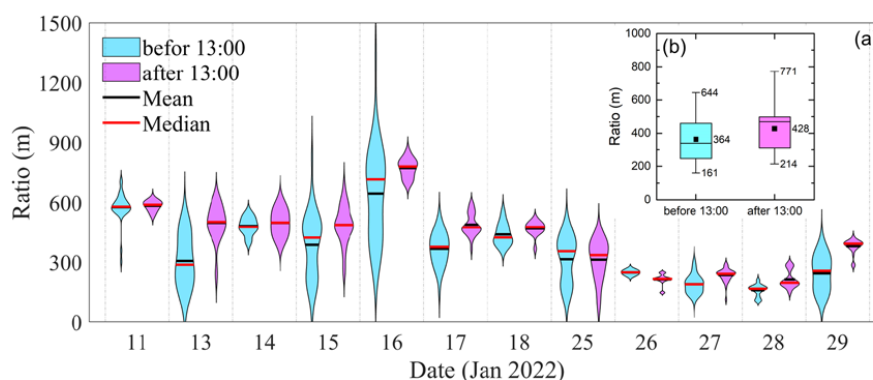


Figure 7. (a) Violin plots of the ratio of TC and NS NO₂ concentrations for each day when observations were available in January 2022, where the data were differentiated between morning (before 13:00 LT) and afternoon (after 13:00LT). (b) The box-whisker plot of the ratio averaged over all observations before and after 13:00 in January 2022. The horizontal lines in the boxes and the top and bottom edges represent the mean and



upper and lower quartile values of the Ratio, the solid square dots represent the median values, and the bars represent the minimum and maximum values.

4 Conclusion and Discussion

Total column and near surface NO₂ data observed during the winter field experiment from Jan 10 to Jan 29, 2022, at the Beijing RADi site were analyzed together with lidar, PM_{2.5} and meteorological data, satellite data, weather maps and air mass trajectories. Based on these observations, the experimental period was sub-divided into three periods: intermittent pollution days, persistent pollution days and clean days. The analysis of the TC and NS NO₂ concentrations shows substantial differences between the first and third period, while during the second period with persistent pollution no TC NO₂ observations were available due to the presence of clouds. During the first period, two episodes with high pollution were identified and analyzed in detail with a focus on the ratio between the variations of the TC and NS NO₂ concentrations and their ratio. The relations between the TC and NS NO₂ concentrations in the morning and in the afternoon, split at 13:00 LT, appear to be significantly different. These differences have been explained in terms of boundary layer dynamics, using lidar data showing the vertical stratification with disconnected boundary layers at different heights in the morning which connected as the boundary layer develops in the afternoon. In addition, the 4-layer NO₂ column concentrations obtained from Pandora show good agreement with the lidar signal in terms of the temporal and vertical variations of the NO₂ concentrations, with differences attributed to the vertical resolution of the Pandora and lidar observations, as well as physical properties of NO₂ and aerosols. From this, together with air mass trajectories, weather maps and TROPOMI satellite observations of the NO₂ spatial distribution, a consistent picture was created showing different source regions for disconnected airmasses arriving at different heights and different times of the day.

Data from the full experimental period, with 12 days for which valid data are available, were analyzed in detail to obtain more insight into the variation of the ratio between the TC and NS NO₂ concentrations. This ratio appears to be overall smaller in the morning



684 than in the afternoon, with larger standard deviations. In addition, the ratios and their
685 standard deviations were overall larger during the more polluted episode I than during
686 the relatively clean period III.

687 Time-continuous remote sensing observations of Pandora were used in this study and
688 the results confirm its possible importance in understanding changes in the distribution
689 of NO₂ in the vertical direction. The NO₂ vertical distribution has been analyzed using
690 less than 3 weeks of observation data, which has some limitations, but the research idea
691 is worthy of reference and promotion. In the future, the implementation of larger-scale
692 experiments in different typical regions and seasons will help to provide further
693 understanding of the ideas presented in this study and improve the shortcomings.

694 The overall conclusion from this study during a relatively short period of almost 3
695 weeks in the winter in Beijing is that the variation between the total column and near
696 surface NO₂ concentrations varies with the concentration level and the time of day. In
697 the afternoon the boundary layer is well developed and satellite observations are
698 sensitive to the NS concentrations, whereas in the morning this depends on
699 meteorological conditions. Hence, satellites with an afternoon overpass are capable to
700 measure TC NO₂ which is representative for NS concentrations, whereas observations
701 earlier in the day may not be. This could possibly affect the interpretation of diurnal
702 variations derived from observations using geostationary satellite.

703

704

705 **Data availability.** Data will be made available on request.

706 **Author contributions.** YZ and YW conceived and designed the study. OL processed
707 the Pandora data. YC collected and processed the meteorological data. YL processed
708 the Lidar data. YZ and GL prepared the paper with contributions from all coauthors. Y-
709 XZ and ZL provide project funding.

710 **Competing interests.** The authors declare that they have no conflict of interest.

711 **Acknowledgements.** We thank the HYSPLIT development and maintenance team, the
712 Beijing RADi site maintainers, and the TROPOMI product development and



713 maintenance team for their support. The PGN is a bilateral project supported with
 714 funding from NASA and ESA.

715 **Financial support.** This work was supported by the National Key Research and
 716 Development Program (2022YFE0209500), the National Natural Science Foundation
 717 of China (4210011039) and the Chinese Academy of Sciences President's International
 718 Fellowship Initiative. Grant No. 2025PVA0014.

719

720 References

- 721 Atkinson, R.: Atmospheric chemistry of VOCs and NO_x, Atmospheric Environment,
 722 34, 2063-2101, [https://doi.org/10.1016/S1352-2310\(99\)00460-4](https://doi.org/10.1016/S1352-2310(99)00460-4), 2000.
- 723 BAM 1020 particulate monitor operation manual (2020), Met One Instruments, Inc.
 724 [https://metone.com/wp-content/uploads/2020/09/BAM-1020-9805-Manual-Rev-](https://metone.com/wp-content/uploads/2020/09/BAM-1020-9805-Manual-Rev-C.pdf)
 725 [C.pdf](https://metone.com/wp-content/uploads/2020/09/BAM-1020-9805-Manual-Rev-C.pdf).
- 726 Boersma, K. F., Jacob, D. J., Trainic, M., Rudich, Y., DeSmedt, I., Dirksen, R., and
 727 Eskes, H. J.: Validation of urban NO₂ concentrations and their diurnal and seasonal
 728 variations observed from the SCIAMACHY and OMI sensors using in situ surface
 729 measurements in Israeli cities, Atmos. Chem. Phys., 9, 3867-3879, 10.5194/acp-
 730 9-3867-2009, 2009.
- 731 Burrows, J. P., Weber, M., Buchwitz, M., Rozanov, V., Ladstätter-Weissenmayer, A.,
 732 Richter, A., DeBeek, R., Hoogen, R., Bramstedt, K., Eichmann, K.-U., Eisinger,
 733 M., and Perner, D.: The Global Ozone Monitoring Experiment (GOME): Mission
 734 Concept and First Scientific Results, Journal of the Atmospheric Sciences, 56,
 735 151-175, [https://doi.org/10.1175/1520-](https://doi.org/10.1175/1520-0469(1999)056<0151:TGOMEG>2.0.CO;2)
 736 [0469\(1999\)056<0151:TGOMEG>2.0.CO;2](https://doi.org/10.1175/1520-0469(1999)056<0151:TGOMEG>2.0.CO;2), 1999.
- 737 Chang, L. S., Kim, D., Hong, H., Kim, D. R., Yu, J. A., Lee, K., Lee, H., Kim, D., Hong,
 738 J., Jo, H. Y., and Kim, C. H.: Evaluation of correlated Pandora column NO₂ and in
 739 situ surface NO₂ measurements during GMAP campaign, Atmos. Chem. Phys.,
 740 22, 10703-10720, 10.5194/acp-22-10703-2022, 2022.
- 741 Cede, A. (2024). Manual for Blick Software Suite 1.8; Manual version 1.8-5, 14 Aug
 742 2024 (202 pp.) available from [https://www.pandonia-global-network.org/wp-](https://www.pandonia-global-network.org/wp-content/uploads/2024/08/BlickSoftwareSuite_Manual_v1-8-5.pdf)
 743 [content/uploads/2024/08/BlickSoftwareSuite_Manual_v1-8-5.pdf](https://www.pandonia-global-network.org/wp-content/uploads/2024/08/BlickSoftwareSuite_Manual_v1-8-5.pdf) (last visited 21
 744 January, 2025)
- 745 Chen, Z.-Y., Zhang, T.-H., Zhang, R., Zhu, Z.-M., Yang, J., Chen, P.-Y., Ou, C.-Q., and
 746 Guo, Y.: Extreme gradient boosting model to estimate PM_{2.5} concentrations with
 747 missing-filled satellite data in China, Atmospheric Environment, 202, 180-189,
 748 <https://doi.org/10.1016/j.atmosenv.2019.01.027>, 2019.
- 749 Cheng, N., Li, Y., Sun, F., Chen, C., Wang, B., Li, Q., Wei, P., and Cheng, B.: Ground-
 750 Level NO₂ in Urban Beijing: Trends, Distribution, and Effects of Emission
 751 Reduction Measures, Aerosol and Air Quality Research, 18, 343-356,



- 10.4209/aaqr.2017.02.0092, 2018.
- de Leeuw, G., van der A, R., Bai, J., Xue, Y., Varotsos, C., Li, Z., Fan, C., Chen, X.,
 Christodoulakis, I., Ding, J., Hou, X., Kouremadas, G., Li, D., Wang, J., Zara, M.,
 Zhang, K., and Zhang, Y.: Air Quality over China, 10.3390/rs13173542, 2021.
- Ding, J., van der A, R. J., Mijling, B., Jalkanen, J.-P., Johansson, L., and Levelt, P. F.:
 Maritime NO_x Emissions Over Chinese Seas Derived From Satellite Observations,
 Geophysical Research Letters, 45, 2031-2037,
<https://doi.org/10.1002/2017GL076788>, 2018.
- Dou, X., Liao, C., Wang, H., Huang, Y., Tu, Y., Huang, X., Peng, Y., Zhu, B., Tan, J.,
 Deng, Z., Wu, N., Sun, T., Ke, P., and Liu, Z.: Estimates of daily ground-level NO₂
 concentrations in China based on Random Forest model integrated K-means,
 Advances in Applied Energy, 2, 100017,
<https://doi.org/10.1016/j.adapen.2021.100017>, 2021.
- Draxler, R. R.: An Overview of the HYSPLIT_4 Modelling System for Trajectories,
 Dispersion, and Deposition,
<https://www.arl.noaa.gov/documents/reports/MetMag.pdf>, 1998.
- Duncan, B. N., Lamsal, L. N., Thompson, A. M., Yoshida, Y., Lu, Z., Streets, D. G.,
 Hurwitz, M. M., and Pickering, K. E.: A space-based, high-resolution view of
 notable changes in urban NO_x pollution around the world (2005–2014), Journal
 of Geophysical Research: Atmospheres, 121, 976-996,
<https://doi.org/10.1002/2015JD024121>, 2016.
- Eum, K.-D., Kazemiparkouhi, F., Wang, B., Manjourides, J., Pun, V., Pavlu, V., and Suh,
 H.: Long-term NO₂ exposures and cause-specific mortality in American older
 adults, Environment International, 124, 10-15,
<https://doi.org/10.1016/j.envint.2018.12.060>, 2019.
- Eum, K.-D., Honda, T. J., Wang, B., Kazemiparkouhi, F., Manjourides, J., Pun, V. C.,
 Pavlu, V., and Suh, H.: Long-term nitrogen dioxide exposure and cause-specific
 mortality in the U.S. Medicare population, Environmental Research, 207, 112154,
<https://doi.org/10.1016/j.envres.2021.112154>, 2022.
- Fan, C., Li, Z., Li, Y., Dong, J., van der A, R., and de Leeuw, G.: Variability of NO₂
 concentrations over China and effect on air quality derived from satellite and
 ground-based observations, Atmos. Chem. Phys., 21, 7723-7748, 10.5194/acp-21-
 7723-2021, 2021.
- Flynn, C. M., Pickering, K. E., Crawford, J. H., Lamsal, L., Krotkov, N., Herman, J.,
 Weinheimer, A., Chen, G., Liu, X., Szykman, J., Tsay, S.-C., Loughner, C., Hains,
 J., Lee, P., Dickerson, R. R., Stehr, J. W., and Brent, L.: Relationship between
 column-density and surface mixing ratio: Statistical analysis of O₃ and NO₂ data
 from the July 2011 Maryland DISCOVER-AQ mission, Atmospheric
 Environment, 92, 429-441, <https://doi.org/10.1016/j.atmosenv.2014.04.041>, 2014.
- Goldberg, D. L., Anenberg, S. C., Kerr, G. H., Mohegh, A., Lu, Z., and Streets, D. G.:
 TROPOMI NO₂ in the United States: A Detailed Look at the Annual Averages,
 Weekly Cycles, Effects of Temperature, and Correlation With Surface NO₂
 Concentrations, Earth's Future, 9, e2020EF001665,
<https://doi.org/10.1029/2020EF001665>, 2021.



- Herman, J., Cede, A., Spinei, E., Mount, G., Tzortziou, M., and Abuhassan, N.: NO₂ column amounts from ground-based Pandora and MFDOAS spectrometers using the direct-sun DOAS technique: Intercomparisons and application to OMI validation, *Journal of Geophysical Research: Atmospheres*, 114, <https://doi.org/10.1029/2009JD011848>, 2009.
- Herman, J., Abuhassan, N., Kim, J., Kim, J., Dubey, M., Raponi, M., and Tzortziou, M.: Underestimation of column NO₂ amounts from the OMI satellite compared to diurnally varying ground-based retrievals from multiple PANDORA spectrometer instruments, *Atmos. Meas. Tech.*, 12, 5593–5612, 10.5194/amt-12-5593-2019, 2019.
- Huang, X., Yang, K., Kondragunta, S., Wei, Z., Valin, L., Szykman, J., and Goldberg, M.: NO₂ retrievals from NOAA-20 OMPS: Algorithm, evaluation, and observations of drastic changes during COVID-19, *Atmospheric Environment*, 290, 119367, <https://doi.org/10.1016/j.atmosenv.2022.119367>, 2022.
- Ialongo, I., Virta, H., Eskes, H., Hovila, J., and Douros, J.: Comparison of TROPOMI/Sentinel-5 Precursor NO₂ observations with ground-based measurements in Helsinki, *Atmos. Meas. Tech.*, 13, 205–218, 10.5194/amt-13-205-2020, 2020.
- Jiang, L., Chen, Y., Zhou, H., and He, S.: NO_x emissions in China: Temporal variations, spatial patterns and reduction potentials, *Atmospheric Pollution Research*, 11, 1473–1480, <https://doi.org/10.1016/j.apr.2020.06.003>, 2020.
- Knepp, T., Pippin, M., Crawford, J., Chen, G., Szykman, J., Long, R., Cowen, L., Cede, A., Abuhassan, N., Herman, J., Delgado, R., Compton, J., Berkoff, T., Fishman, J., Martins, D., Stauffer, R., Thompson, A. M., Weinheimer, A., Knapp, D., Montzka, D., Lenschow, D., and Neil, D.: Estimating surface NO₂ and SO₂ mixing ratios from fast-response total column observations and potential application to geostationary missions, *Journal of Atmospheric Chemistry*, 72, 261–286, 10.1007/s10874-013-9257-6, 2015.
- KNMI (2017), Algorithm theoretical basis document for the TROPOMI L01b data processor, Tech. Rep. S5P-KNMI-L01B 0009-SD, Koninklijk Nederlands Meteorologisch Instituut (KNMI), CI-6480-ATBD, issue 8.0.0, available at: <https://sentinels.copernicus.eu/documents/247904/2476257/Sentinel-5P-TROPOMI-Level-1B-ATBD> (last access: 11 January 2020).
- Kornartit, C., Sokhi, R. S., Burton, M. A., and Ravindra, K.: Activity pattern and personal exposure to nitrogen dioxide in indoor and outdoor microenvironments, *Environment International*, 36, 36–45, <https://doi.org/10.1016/j.envint.2009.09.004>, 2010.
- Lamsal, L. N., Krotkov, N. A., Celarier, E. A., Swartz, W. H., Pickering, K. E., Bucsela, E. J., Gleason, J. F., Martin, R. V., Philip, S., Irie, H., Cede, A., Herman, J., Weinheimer, A., Szykman, J. J., and Knepp, T. N.: Evaluation of OMI operational standard NO₂ column retrievals using in situ and surface-based NO₂ observations, *Atmos. Chem. Phys.*, 14, 11587–11609, 10.5194/acp-14-11587-2014, 2014.
- Levelt, P. F., Oord, G. H. J. v. d., Dobber, M. R., Malkki, A., Huib, V., Johan de, V., Stammes, P., Lundell, J. O. V., and Saari, H.: The ozone monitoring instrument,



- IEEE Transactions on Geoscience and Remote Sensing, 44, 1093-1101, 10.1109/TGRS.2006.872333, 2006.
- Li, J., Wang, Y., Zhang, R., Smeltzer, C., Weinheimer, A., Herman, J., Boersma, K. F., Celarier, E. A., Long, R. W., Szykman, J. J., Delgado, R., Thompson, A. M., Knepp, T. N., Lamsal, L. N., Janz, S. J., Kowalewski, M. G., Liu, X., and Nowlan, C. R.: Comprehensive evaluations of diurnal NO₂ measurements during DISCOVER-AQ 2011: effects of resolution-dependent representation of NO_x emissions, Atmos. Chem. Phys., 21, 11133-11160, 10.5194/acp-21-11133-2021, 2021.
- Liu, O., Li, Z., Lin, Y., Fan, C., Zhang, Y., Li, K., Zhang, P., Wei, Y., Chen, T., Dong, J., and de Leeuw, G.: Evaluation of the first year of Pandora NO₂ measurements over Beijing and application to satellite validation, Atmos. Meas. Tech., 17, 377-395, 10.5194/amt-17-377-2024, 2024.
- Model 42i Trace Level Manual (2007). https://cires1.colorado.edu/jimenez-group/Manuals/Manual_NOx_42i.pdf.
- Nordeide Kuiper, I., Svanes, C., Markevych, I., Accordini, S., Bertelsen, R. J., Bråbäck, L., Heile Christensen, J., Forsberg, B., Halvorsen, T., Heinrich, J., Hertel, O., Hoek, G., Holm, M., de Hoogh, K., Janson, C., Malinowski, A., Marcon, A., Miodini Nilsen, R., Sigsgaard, T., and Johannessen, A.: Lifelong exposure to air pollution and greenness in relation to asthma, rhinitis and lung function in adulthood, Environment International, 146, 106219, <https://doi.org/10.1016/j.envint.2020.106219>, 2021.
- Qin, K., Rao, L., Xu, J., Bai, Y., Zou, J., Hao, N., Li, S., and Yu, C.: Estimating Ground Level NO₂ Concentrations over Central-Eastern China Using a Satellite-Based Geographically and Temporally Weighted Regression Model, 10.3390/rs9090950, 2017.
- Qin, K., Han, X., Li, D., Xu, J., Loyola, D., Xue, Y., Zhou, X., Li, D., Zhang, K., and Yuan, L.: Satellite-based estimation of surface NO₂ concentrations over east-central China: A comparison of POMINO and OMNO2d data, Atmospheric Environment, 224, 117322, <https://doi.org/10.1016/j.atmosenv.2020.117322>, 2020.
- Reed, A. J., Thompson, A. M., Kollonige, D. E., Martins, D. K., Tzortziou, M. A., Herman, J. R., Berkoff, T. A., Abuhassan, N. K., and Cede, A.: Effects of local meteorology and aerosols on ozone and nitrogen dioxide retrievals from OMI and pandora spectrometers in Maryland, USA during DISCOVER-AQ 2011, Journal of Atmospheric Chemistry, 72, 455-482, 10.1007/s10874-013-9254-9, 2015.
- Sandradewi, J., Prévôt, A. S. H., Szidat, S., Perron, N., Alfarra, M. R., Lanz, V. A., Weingartner, E., and Baltensperger, U.: Using aerosol light absorption measurements for the quantitative determination of wood burning and traffic emission contributions to particulate matter, Environmental science & technology, 42 9, 3316-3323, 2008.
- Scientific, M. (2016). Aethalometer Model AE33 User Manual, version 1.54. Aerosol doo, Ljubljana, Slovenia. https://gml.noaa.gov/aftp/aerosol/doc/manuals/AE33_UsersManual_Rev154.pdf.
- Sorek-Hamer, M., Strawa, A. W., Chatfield, R. B., Esswein, R., Cohen, A., and Broday,



- 884 D. M.: Improved retrieval of PM_{2.5} from satellite data products using non-linear
 885 methods, *Environmental Pollution*, 182, 417-423,
 886 <https://doi.org/10.1016/j.envpol.2013.08.002>, 2013.
- 887 Stein, A. F., Draxler, R. R., Rolph, G. D., Stunder, B. J. B., Cohen, M. D., and Ngan, F.:
 888 NOAA's HYSPLIT Atmospheric Transport and Dispersion Modeling System,
 889 *Bulletin of the American Meteorological Society*, 96, 2059-2077,
 890 <https://doi.org/10.1175/BAMS-D-14-00110.1>, 2015.
- 891 Stull, R.B.: *An Introduction to Boundary Layer Meteorology*. Kluwer Academic
 892 Publishers, Dordrecht, The Netherlands. (666 pp.). ISBN 90-227-2768-6.
 893 <https://doi.org/10.1007/978-94-009-3027-8>, 1988.
- 894 Tang, T., Cheng, T., Zhu, H., Ye, X., Fan, D., Li, X., and Tong, H.: Quantifying
 895 instantaneous nitrogen oxides emissions from power plants based on space
 896 observations, *Science of The Total Environment*, 938, 173479,
 897 <https://doi.org/10.1016/j.scitotenv.2024.173479>, 2024.
- 898 Tzortziou, M., Herman, J. R., Cede, A., Loughner, C. P., Abuhassan, N., and Naik, S.:
 899 Spatial and temporal variability of ozone and nitrogen dioxide over a major urban
 900 estuarine ecosystem, *Journal of Atmospheric Chemistry*, 72, 287-309,
 901 [10.1007/s10874-013-9255-8](https://doi.org/10.1007/s10874-013-9255-8), 2015.
- 902 Tzortziou, M., Parker, O., Lamb, B., Herman, J. R., Lamsal, L., Stauffer, R., and
 903 Abuhassan, N.: Atmospheric Trace Gas (NO₂ and O₃) Variability in South Korean
 904 Coastal Waters, and Implications for Remote Sensing of Coastal Ocean Color
 905 Dynamics, *Remote Sensing*, 10, 3390, [10.3390/rs10101587](https://doi.org/10.3390/rs10101587), 2018.
- 906 van der A, R. J., Peters, D. H. M. U., Eskes, H., Boersma, K. F., Van Roozendael, M.,
 907 De Smedt, I., and Kelder, H. M.: Detection of the trend and seasonal variation in
 908 tropospheric NO₂ over China, *Journal of Geophysical Research: Atmospheres*, 111,
 909 <https://doi.org/10.1029/2005JD006594>, 2006.
- 910 van der A, R. J., Mijling, B., Ding, J., Koukouli, M. E., Liu, F., Li, Q., Mao, H., and
 911 Theys, N.: Cleaning up the air: effectiveness of air quality policy for SO₂ and NO_x
 912 emissions in China, *Atmos. Chem. Phys.*, 17, 1775-1789, [10.5194/acp-17-1775-](https://doi.org/10.5194/acp-17-1775-2017)
 913 2017, 2017.
- 914 van Geffen, J. H. G. M., Eskes, H. J., Boersma, K. F., Maasakkers, J. D., and Veefkind,
 915 J. P. (2019), TROPOMI ATBD of the total and tropospheric NO₂ data products,
 916 Tech. Rep. S5P-KNMI-L2-0005-RP, Koninklijk Nederlands Meteorologisch
 917 Instituut (KNMI), CI-7430-ATBD, issue 1.4.0, available at:
 918 [https://sentinels.copernicus.eu/documents/247904/2476257/Sentinel-5P-](https://sentinels.copernicus.eu/documents/247904/2476257/Sentinel-5P-TROPOMI-ATBD-NO2-data-products)
 919 TROPOMI-ATBD-NO₂-data-products (last access: 11 January 2020).
- 920 van Geffen, J. H. G. M., Boersma, K. F., Van Roozendael, M., Hendrick, F., Mahieu,
 921 E., De Smedt, I., Snee, M., and Veefkind, J. P.: Improved spectral fitting of
 922 nitrogen dioxide from OMI in the 405–465 nm window, *Atmos. Meas. Tech.*, 8,
 923 1685-1699, [10.5194/amt-8-1685-2015](https://doi.org/10.5194/amt-8-1685-2015), 2015.
- 924 Veefkind, J. P., Aben, I., McMullan, K., Förster, H., de Vries, J., Otter, G., Claas, J.,
 925 Eskes, H. J., de Haan, J. F., Kleipool, Q., van Weele, M., Hasekamp, O.,
 926 Hoogeveen, R., Landgraf, J., Snel, R., Tol, P., Ingmann, P., Voors, R., Kruizinga,
 927 B., Vink, R., Visser, H., and Levelt, P. F.: TROPOMI on the ESA Sentinel-5



- 928 Precursor: A GMES mission for global observations of the atmospheric
 929 composition for climate, air quality and ozone layer applications, *Remote Sensing*
 930 of Environment, 120, 70-83, <https://doi.org/10.1016/j.rse.2011.09.027>, 2012.
- 931 Wang, Y., Dörner, S., Donner, S., Böhnke, S., De Smedt, I., Dickerson, R. R., Dong, Z.,
 932 He, H., Li, Z., Li, Z., Li, D., Liu, D., Ren, X., Theys, N., Wang, Y., Wang, Y., Wang,
 933 Z., Xu, H., Xu, J., and Wagner, T.: Vertical profiles of NO₂, SO₂, HONO, HCHO,
 934 CHOCHO and aerosols derived from MAX-DOAS measurements at a rural site in
 935 the central western North China Plain and their relation to emission sources and
 936 effects of regional transport, *Atmos. Chem. Phys.*, 19, 5417-5449, 10.5194/acp-
 937 19-5417-2019, 2019.
- 938 Wei, J., Liu, S., Li, Z., Liu, C., Qin, K., Liu, X., Pinker, R. T., Dickerson, R. R., Lin, J.,
 939 Boersma, K. F., Sun, L., Li, R., Xue, W., Cui, Y., Zhang, C., and Wang, J.: Ground-
 940 Level NO₂ Surveillance from Space Across China for High Resolution Using
 941 Interpretable Spatiotemporally Weighted Artificial Intelligence, *Environmental*
 942 *Science & Technology*, 56, 9988-9998, 10.1021/acs.est.2c03834, 2022.
- 943 Xing, C., Liu, C., Wang, S., Chan, K. L., Gao, Y., Huang, X., Su, W., Zhang, C., Dong,
 944 Y., Fan, G., Zhang, T., Chen, Z., Hu, Q., Su, H., Xie, Z., and Liu, J.: Observations
 945 of the vertical distributions of summertime atmospheric pollutants and the
 946 corresponding ozone production in Shanghai, China, *Atmos. Chem. Phys.*, 17,
 947 14275-14289, 10.5194/acp-17-14275-2017, 2017.
- 948 Zhang, C., Liu, C., Li, B., Zhao, F., and Zhao, C.: Spatiotemporal neural network for
 949 estimating surface NO₂ concentrations over north China and their human health
 950 impact, *Environmental Pollution*, 307, 119510,
 951 <https://doi.org/10.1016/j.envpol.2022.119510>, 2022.
- 952 Zhang, Y., Wang, Y., Chen, G., Smeltzer, C., Crawford, J., Olson, J., Szykman, J.,
 953 Weinheimer, A. J., Knapp, D. J., Montzka, D. D., Wisthaler, A., Mikoviny, T., Fried,
 954 A., and Diskin, G.: Large vertical gradient of reactive nitrogen oxides in the
 955 boundary layer: Modeling analysis of DISCOVER-AQ 2011 observations, *Journal*
 956 *of Geophysical Research: Atmospheres*, 121, 1922-1934,
 957 <https://doi.org/10.1002/2015JD024203>, 2016.
- 958 Zhao, R., Gu, X., Xue, B., Zhang, J., and Ren, W.: Short period PM_{2.5} prediction based
 959 on multivariate linear regression model, *PLOS ONE*, 13, e0201011,
 960 10.1371/journal.pone.0201011, 2018.
- 961 Zhao, Z., Lu, Y., Zhan, Y., Cheng, Y., Yang, F., Brook, J. R., and He, K.: Long-term
 962 spatiotemporal variations in surface NO₂ for Beijing reconstructed from surface
 963 data and satellite retrievals, *Science of The Total Environment*, 904, 166693,
 964 <https://doi.org/10.1016/j.scitotenv.2023.166693>, 2023.
- 965 Zhao, X., Griffin, D., Fioletov, V., McLinden, C., Cede, A., Tiefengraber, M., Müller,
 966 M., Bogner, K., Strong, K., Boersma, F., Eskes, H., Davies, J., Ogyu, A., and Lee,
 967 S. C.: Assessment of the quality of TROPOMI high-spatial-resolution NO₂ data
 968 products in the Greater Toronto Area, *Atmos. Meas. Tech.*, 13, 2131-2159,
 969 10.5194/amt-13-2131-2020, 2020.